Article

Cell Reports

Cancer Cells Resist Mechanical Destruction in Circulation via RhoA/Actomyosin-Dependent Mechano-Adaptation

Graphical Abstract

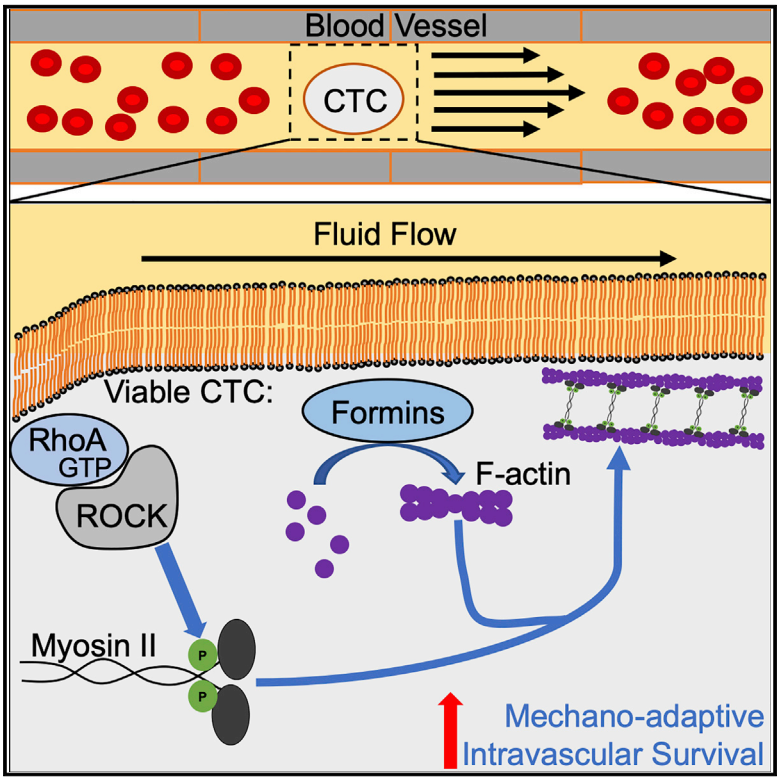

Highlights

- Cancer cells from primary tumors are resistant to fluid shear stress (FSS)
- Resistance to FSS is a physiological, mechano-adaptive response in cancer cells
- Cancer cells respond to FSS by activating the RhoA-myosin II axis and formins
- Myosin II activity protects CTCs from hemodynamic forces in *in vivo* assays

Authors

Devon L. Moose, Benjamin L. Krog, Tae-Hyung Kim, ..., Christopher S. Stipp, Amy C. Rowat, Michael D. Henry

Correspondence

michael-henry@uiowa.edu

In Brief

Moose et al. show that cancer cells exhibit a mechano-adaptive response to fluid shear stress through activation of the RhoA-actomyosin signaling axis. Utilizing *in vivo* models, they extend these findings to demonstrate that this axis maintains intravascular survival of circulating tumor cells (CTCs) that contributes to the development of metastasis.

Moose et al., 2020, Cell Reports *30*, 3864–3874
March 17, 2020
https://doi.org/10.1016/j.celrep.2020.02.080

CellPress

OPEN ACCESS
CellPress

Cell Reports
Article

Cancer Cells Resist Mechanical Destruction in Circulation via RhoA/Actomyosin-Dependent Mechano-Adaptation

Devon L. Moose,[1,2] Benjamin L. Krog,[1,3] Tae-Hyung Kim,[4] Lei Zhao,[1] Sophia Williams-Perez,[5] Gretchen Burke,[1] Lillian Rhodes,[1] Marion Vanneste,[1] Patrick Breheny,[6] Mohammed Milhem,[7,8] Christopher S. Stipp,[1,7,9] Amy C. Rowat,[4] and Michael D. Henry[1,2,7,10,11,*]

[1]Department of Molecular Physiology and Biophysics, Carver College of Medicine, University of Iowa, Iowa City, IA 52242, USA
[2]Cancer Biology Program, Biomedical Sciences, University of Iowa, Iowa City, IA 52242, USA
[3]Department of Biomedical Engineering, College of Engineering, University of Iowa, Iowa City, IA 52242, USA
[4]Department of Integrative Biology and Physiology, University of California, Los Angeles, Los Angeles, CA 90095, USA
[5]Carver College of Medicine, University of Iowa, Iowa City, IA 52242, USA
[6]Department of Biostatistics, College of Public Health, University of Iowa, Iowa City, IA 52242, USA
[7]Holden Comprehensive Cancer Center, Iowa City, IA 52242, USA
[8]Division of Hematology and Oncology, Internal Medicine, Carver College of Medicine, University of Iowa, Iowa City, IA 52242, USA
[9]Department of Biology, University of Iowa, Iowa City, IA 52242, USA
[10]Departments of Pathology, Urology and Radiation Oncology, Carver College of Medicine, University of Iowa, Iowa City, IA 52242, USA
[11]Lead Contact
*Correspondence: michael-henry@uiowa.edu
https://doi.org/10.1016/j.celrep.2020.02.080

SUMMARY

During metastasis, cancer cells are exposed to potentially destructive hemodynamic forces including fluid shear stress (FSS) while *en route* to distant sites. However, prior work indicates that cancer cells are more resistant to brief pulses of high-level FSS *in vitro* relative to non-transformed epithelial cells. Herein, we identify a mechano-adaptive mechanism of FSS resistance in cancer cells. Our findings demonstrate that cancer cells activate RhoA in response to FSS, which protects them from FSS-induced plasma membrane damage. We show that cancer cells freshly isolated from mouse and human tumors are resistant to FSS, that formin and myosin II activity protects circulating tumor cells (CTCs) from destruction, and that short-term inhibition of myosin II delays metastasis in mouse models. Collectively, our data indicate that viable CTCs actively resist destruction by hemodynamic forces and are likely to be more mechanically robust than is commonly thought.

INTRODUCTION

Circulating tumor cells (CTCs) are a blood-borne intermediate in the metastatic cascade that are necessary for colonizing distant organ sites. Tumors may generate millions of CTCs per day, but seminal work in cancer biology has established the concept of "metastatic inefficiency" whereby only a small fraction of these CTCs go on to generate clinically observable metastases (Fidler, 1970; Weiss, 1990; Zeidman et al., 1950). CTCs exist in a fluid microenvironment quite distinct from that of the solid tumor; in the circulation, these cells are exposed to various biological and mechanical stresses that may lead to their demise, including detachment from extracellular matrix, removal from the trophic factors within the primary tumor, newfound contact with the immune system, and exposure to hemodynamic forces (Labelle and Hynes, 2012; Strilic and Offermanns, 2017). Hemodynamic stresses include fluid shear stress (FSS), shear and compressive stresses due to deformation in the microcirculation, and under some circumstances, traction stresses generated by adherence to the endothelium (Wirtz et al., 2011). Circulatory FSS ranges across 4 orders of magnitude, from less than 1 dyne/cm^2 in lymphatic vessels and the microcirculation to over 1,000 dynes/cm^2 in turbulent flows in the heart and in certain pathological settings (Antiga and Steinman, 2009; Dixon et al., 2006; Popel and Johnson, 2005; Strony et al., 1993). Perhaps because cancer cells derived from solid tissues appear to lack adaptations in membrane and cytoskeletal features that allow blood cells to withstand hemodynamic forces (Mohandas and Evans, 1994), it has often been suggested that CTCs are mechanically fragile relative to blood cells. Indeed, a number of studies indicate that many CTCs are dead or dying (Kallergi et al., 2013; Larson et al., 2004; Méhes et al., 2001; Swartz et al., 1999). However, it is not clear whether death of CTCs is a consequence of the biological and mechanical stresses outlined above or the methods by which CTCs are isolated. It is also possible that many CTCs arrive in the circulation as dead or dying cells, having been passively shed from tumors (Swartz et al., 1999). Thus, whether viable CTCs are mechanically fragile is still a matter of speculation.

Other experimental evidence suggests that CTCs may be mechanically robust. For example, studies in mouse models indicate that cancer cells injected into various vascular compartments survive their initial exposure to the circulation, with 85%–98% of injected cells viable and arrested in the microcirculation within minutes following injection (Cameron et al., 2000; Fidler,

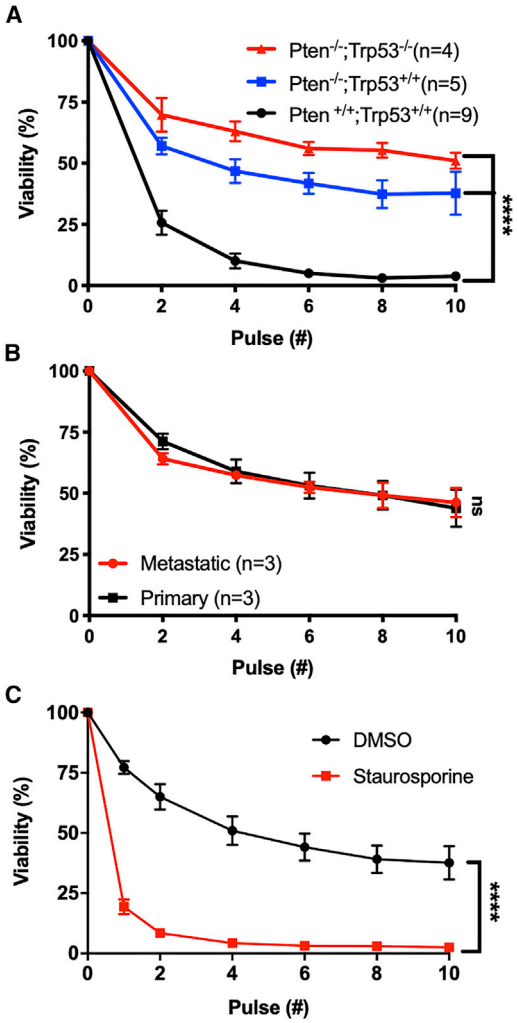

Figure 1. Viable Tumor Cells Are Resistant to FSS

(A) Effects of 2–10 FSS pulses on the viability of freshly isolated prostate cancer cells from tumor-bearing mice ($Pten^{-/-}$ and $Pten^{-/-}$;$Trp53^{-/-}$) and on wild-type prostate epithelial cells (****$p < 0.0001$, two-way ANOVA).

(B) Effects of 2–10 FSS pulses on cells derived from primary and metastatic human melanoma PDX tumors ($p > 0.05$, two-way ANOVA).

(C) Effects of staurosporine treatment versus vehicle only (DMSO) on FSS resistance (****$p < 0.0001$, n = 4; two-way ANOVA, n = 3). Data are presented as mean with SEM error bars.

See also Figure S1.

1970; Luzzi et al., 1998; Mizuno et al., 1998; Qian et al., 2009). Association of CTCs with blood components such as platelets or CTC clusters may, in principle, afford mechanical protection to CTCs, but there is little direct evidence to support this (Egan et al., 2014). Cell-intrinsic mechanisms may also contribute to CTC survival in response to mechanical challenges. For example, the mechanosensitive pannexin-1 channel mediates survival in response to cell deformation in the microvasculature (Furlow et al., 2015). Moreover, we found that, unlike their non-transformed epithelial counterparts, cancer cells are remarkably resistant to brief pulses of high-level FSS (Barnes et al., 2012), and these findings have since been confirmed and extended by others (Mitchell et al., 2015; Triantafillu et al., 2017; Vennin et al., 2017). More recently, we found that exposure to brief pulses of FSS results in cell stiffening, suggesting that this mechano-adaptive response of cells is related to the FSS resistance phenotype (Chivukula et al., 2015). A role for cellular mechanical properties in FSS response is further substantiated by reports that lamin A/C contributes to FSS resistance (Mitchell et al., 2015). Taken together, these studies define that the FSS resistance phenotype is: (1) evident in cancer cell lines from diverse histologies; (2) conferred by the presence of transforming oncogenes, including *ras*, *myc*, and *PI3K*; (3) comprises rapid and transient mechano-adaptation induced by exposure to FSS; (4) requires the presence of extracellular calcium; and (5) involves the actin cytoskeleton and the activity of Rho kinase. These data led to the hypothesis that cancer cells may actively resist destruction by hemodynamic forces, via changes in cellular mechanics. However, the details of the mechanism underlying FSS resistance have not been described, and whether this feature is functionally relevant for CTCs has not been determined.

RESULTS

Viable Primary Tumor Cells Are Resistant to FSS

Prior studies on FSS resistance analyzed established cancer cell lines, many of which are derived from metastatic tumors (Barnes et al., 2012; Mitchell et al., 2015; Triantafillu et al., 2017; Vennin et al., 2017). To address the possibility that FSS resistance is an artifact of cell culture or the result of metastatic selection, we examined the effects of FSS in tumor cells freshly isolated from a genetically engineered mouse model of prostate cancer and from human melanoma patient-derived xenografts (PDXs). We exposed the cell suspensions to 10 brief (~1 ms) pulses of FSS (τ_{max} = 6,400 dynes/cm^2) and assessed FSS resistance after every second pulse, as previously described (Barnes et al., 2012). Prostate epithelial cells from the tumor-bearing mice displayed greater FSS resistance than those from their wild-type counterparts (Figure 1A). Additionally, we found no difference in FSS resistance between cells isolated from PDX generated from primary and metastatic lesions (Figure 1B). These data demonstrate that FSS resistance is a feature of cancer cells within the primary tumor and not the result of selection during tissue culture or metastasis. Moreover, we observed that FSS resistance was elevated in *Pten*/*Trp53* double-knockout versus *Pten*-only knockout mice (Figure 1A). Given that *Pten*/*Trp53* knockout prostate tumors are known to be markedly more aggressive than their *Pten*-only knockout counterparts (Chen et al., 2005; Svensson et al., 2011), the observed difference suggests that FSS resistance may be influenced by tumor aggressiveness.

Given that several studies have shown that many CTCs are dead or in the process of dying, and published observations on FSS resistance indicate that it is an active mechano-adaptive process, we hypothesized that apparent CTC fragility may be a consequence of cell death. To test this, we induced apoptosis in PC-3 prostate cancer cells by treating them with staurosporine (4 μM, 4 h; confirmed by Annexin V staining) and evaluated FSS resistance (Figure S1A). The staurosporine-treated cells were markedly more sensitive to FSS than their untreated

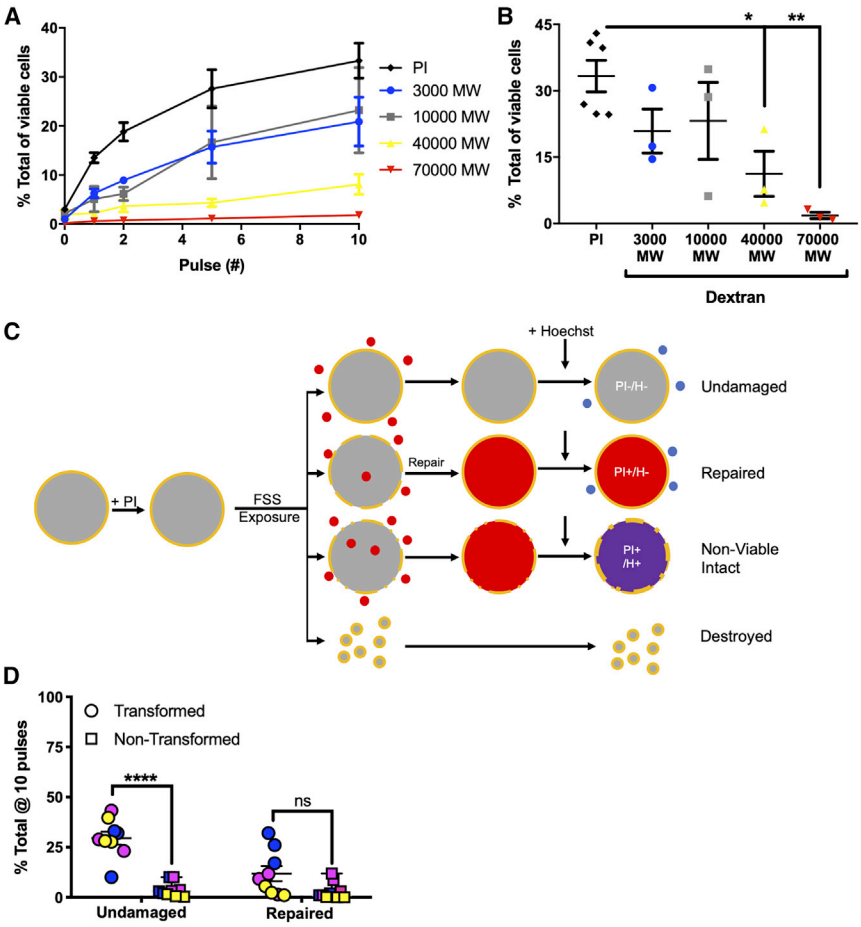

Figure 2. Cancer Cells Resist FSS-Induced Nanometer-Scale Disruption of the Plasma Membrane

(A) Uptake of dextrans of various size and of propidium iodide (PI) in PC-3 cells exposed to FSS.

(B) Uptake after 10 pulses of FSS. Uptake of both 40,000 and 70,000 MW dextrans decreased in comparison with that of PI (*$p < 0.05$ and **$p < 0.01$, respectively; one-way ANOVA with Bonferroni correction).

(C) Schematic of flow cytometry assay for evaluation of undamaged and repaired fraction of cells after exposure to FSS. Shown is sequence of exposure to PI, FSS, and Hoechst dye, making it possible to identify cells that resist membrane damage ($PI^{-}Hoechst^{-}$) and cells that undergo membrane repair ($PI^{+}Hoechst^{-}$).

(D) Effects of 10 FSS pulses on the fraction of cells that are undamaged or have undergone repair for both transformed cancer cells (PC-3, blue circle; MDA-MB-231, pink circle; TCCSUP, yellow circle) and non-transformed cells (PrEC-LH, blue square; MCF-10A, pink square; primary urothelial, yellow square) (***$p < 0.001$, t test, n = 3/cell line). Membrane repair after 10 pulses varied among cell lines and did not differ significantly by transformation status ($p > 0.05$, t test, n = 3/cell line). Data are presented as mean with SEM error bars.

See also Figure S2.

counterparts; most were dead after two pulses (Figure 1C). We also used ionomycin to induce necrotic-like cell death; we found that after a single pulse of FSS, nearly all of the ionomycin-treated cells had been destroyed (Figures S1B and S1C). These data affirm that FSS resistance is an active mechano-adaptive process.

Cancer Cells Are Intrinsically Resistant to Small (<12 nm) Membrane Disruptions Induced by FSS

Our previous study had demonstrated that exposure to FSS results in membrane damage, detected as uptake of the membrane impermeant dye propidium iodide (PI), in otherwise viable PC-3 prostate cancer cells (Barnes et al., 2012). To further characterize the plasma membrane damage produced by our FSS protocol, we exposed PC-3 prostate cancer cells to FSS in the presence of fluorescent dextrans of increasing molecular weight (MW) and evaluated cellular uptake and viability by flow cytometry. As the size of the dextran probe increased from 3,000 to 70,000 MW, progressively less was taken up by viable cells (Figure 2A). After 10 pulses of FSS, less than 5% of cells showed evidence of uptake of 70,000 MW dextran, whereas ~30% had taken up 3,000 MW dextran, consistent with the fraction of viable cells that took up PI (668 MW) (Figure 2B). Since the Stokes diameter of 70,000-MW dextran is ~12 nm (Cui et al., 2010), exposure to FSS in our protocol resulted in relatively small and reparable holes in the plasma membrane of cancer cells. Thus, the FSS resistance of cancer cells could reflect a greater capacity to repair the plasma membrane in response to damage or, alternatively, a greater ability to resist accruing membrane damage than that of non-transformed cells.

To determine the relative importance of plasma membrane repair versus resistance to plasma membrane damage, we developed a flow cytometry-based assay that measures the fraction of viable cells in which membrane damage is repaired or in which no membrane damage occurs (Figures 2C and S2A). Before exposing the cells to FSS, we briefly added PI, and afterward we added counting beads and Hoechst 33258 as a viability dye. Because membrane damage must be repaired rapidly in order to maintain cell viability, cells that repair damage to the plasma membrane will be PI-positive but Hoechst-negative, and undamaged cells will be negative for both dyes. Utilizing this assay, we tested for the capacity of three pairs of cancer and non-transformed cells to resist and repair FSS-induced plasma membrane damage. In the case of the transformed cell lines, PC-3, MDA-MB-231, and TCCSUP, all exhibit a consistent ability to resist plasma membrane damage (33.4%, 31.8%, and 31.8%, respectively) after 10 pulses of FSS (Figures 2D, S2B, S2D, S2F, and S2H). The level of undamaged transformed cells was substantially elevated over that in non-transformed cells, with all three non-transformed cell lines, PrEC-LH, MCF-10A, as well as primary urothelial cells, having less than 5% undamaged fraction after 10 pulses of FSS (Figures 2D, S2C, S2E, S2G, and

S2H). Of the transformed cells that were evaluated, only PC-3 cells had a significant repair fraction (33.5%). Both MDA-MB-231 and TCCSUP displayed only minimal evidence of repair (7.5% and 3.0%) (Figures 2D and S2I). Non-transformed MCF-10A cells showed an appreciable repair fraction during initial pulses that was diminished after 10 pulses, indicating that their susceptibility to damage outweighs their ability to repair damage. Both PrEC-LH and primary urothelial cells exhibited only marginal membrane repair (Figures 2D and S2I). These data demonstrate that, although membrane repair may contribute to FSS resistance of some transformed cell lines, cancer cells are consistently distinguished from non-transformed cells by their ability to resist plasma membrane damage.

Resistance to FSS Depends on RhoA/Actomyosin Activity

To determine the cause of increased resistance to FSS-induced damage in cancer cells, we considered previously published findings suggesting that cell stiffness may contribute to FSS resistance. Those studies demonstrated that: (1) PC-3 cells stiffen in response to FSS (Chivukula et al., 2015), and (2) inhibitors of F-actin and Rho kinase can sensitize cancer cells to FSS (Barnes et al., 2012; Vennin et al., 2017). Based on these findings, we hypothesized that members of the Rho-family GTPases, which regulate actin dynamics and actomyosin contractility, are activated in response to FSS and contribute to the mechano-adaptation of cancer cells to FSS. To test this hypothesis, we utilized RhoA/C and Rac1 GTP pull-down assays. We found that in PC-3 cells, both RhoA and RhoC were activated in response to FSS, whereas active Rac1 levels were similar (Figures 3A, 3B, and S3A–S3D). We then knocked down RhoA and RhoC in a PC-3 derivative cell line and found that only RhoA knockdown cells showed decreased FSS resistance (Figure S3E). Utilizing the RhoA activation assay, we found that FSS exposure activates RhoA in both MDA-MB-231 and TCCSUP cells (Figures 3A and 3B). We also measured RhoA activation in the non-transformed cell lines, PrEC-LH and MCF-10A, and found that neither cell line activated RhoA in response to FSS (Figures S3F and S3G). To determine whether the activation of RhoA is important for cancer cells to maintain an undamaged population, we knocked down RhoA in PC-3 using two different small hairpin RNA (shRNA) constructs in PC-3 cells (Figure S3J) and found that there was a reduction in the ability of the knockdown cells to remain undamaged (Figures 3C, S3H, and S3I).

Because RhoA activation typically leads to increased levels of F-actin (Ridley and Hall, 1992), we assayed for cortical F-actin levels in PC-3 cells after two pulses of FSS exposure by using imaging flow cytometry. This revealed a robust increase in the formation of cortical F-actin, which is consistent with increased RhoA activity (Figures 3D, S4A, and S4B). Because both Arp 2/3 and formins are mechano-responsive (Jégou et al., 2013; Kubota et al., 2017; Risca et al., 2012), we wanted to determine whether either is the likely cause for the increased F-actin in response to FSS. To do this, we exposed PC-3 cells to FSS after incubation with a formin (SMIFH2) or an Arp2/3 (CK-666) inhibitor and measured viability after FSS exposure in comparison with a control (DMSO) (Figure S4C). This experiment showed that formins were more important than Arp2/3 for FSS resistance. This result is consistent with the GTPase activity assays above (Figures 3A, 3B, and S3A–S3D) because formins are regulated by Rho, whereas Arp2/3 is regulated by Rac (Spiering and Hodgson, 2011). We then measured cortical F-actin levels in PC-3 cells treated with SMIFH2 and exposed to FSS, and found that inhibition of formins with SMIFH2 reduced the FSS-induced increase in cortical F-actin (Figure 3E). We also tested whether formin activity is required for cancer cells to resist plasma membrane damage. Across all three cancer cell lines, we found that treatment with the formin inhibitor both reduced the ability of the cells to remain undamaged and also decreased the ability of the cells to repair plasma membrane damage (Figures 3F, S5A, and S5B).

Another well-known function of RhoA is its regulation of non-muscle myosin II activity through direct or indirect promotion of myosin light chain (MLC) phosphorylation (Amano et al., 1996; Kimura et al., 1996). To test whether FSS leads to increased phospho-MLC, we exposed PC-3, MDA-MB-231, and TCCSUP cells to two pulses of FSS and found that there was a modest increase in phospho-MLC in each of those cell lines (Figures 3G and 3H). To test whether the RhoA-myosin II signaling axis is important for FSS resistance, we used blebbistatin to inhibit myosin II activity in PC-3, MDA-MB-231, and TCCSUP cells and found that the fraction of undamaged cells was significantly reduced (Figures 3I, S5C). Similar to RHOA knockdown, the inhibition of myosin II did not significantly alter the fraction of repaired cells after 10 pulses of FSS in all cell lines (Figures 3I, S5D), although after 2 pulses, blebbistatin treatment apparently increased the repair fraction observed in PC-3 and MDA-MB-231 cells, presumably because more cells were being damaged (Figures S3I and S5D). We also utilized inhibitors that target Rho kinase and MLC kinase, and found that these too sensitized PC-3 cells to FSS (Figures S5E and S5F). Importantly, at the exposures used in these studies, none of these pharmacologic agents influenced the viability of cells prior to FSS exposure (Figure S5G). This indicates that the effects of these compounds on FSS resistance are due to specific inhibition of this mechanism rather than a secondary consequence of cytotoxicity.

Inhibition of Myosin II Sensitizes Cancer Cells to Hemodynamic Forces

We next sought to determine the contribution of myosin II to FSS resistance in CTCs *in vivo*. To this end, we adapted a mouse model that had been developed to assess the trapping of viable cells in the lung microvasculature following their injection via the tail vein (Cameron et al., 2000). PC-3 cells were labeled with distinct viable fluorescent dyes, pretreated with either blebbistatin or DMSO (vehicle control), and mixed with 15 μm fluorescent microspheres prior to injection. Following injection, the mice were euthanized within 3 min to assess the short-term effects of the circulation on trapping of intact cells in the lung microvasculature (Figure 4A). We found that the number of intact PC-3 cells lodged in the lungs was significantly lower in the blebbistatin-treated versus DMSO group (49.71% ± 1.57% versus 59.01% ± 2.67%) (Figures 4B–4E; Table S1). Within this experiment we also swapped the dyes used for each treatment condition and found that the results obtained were independent of the dye label used (Figure 4F). This indicated that it was the blebbistatin treatment that led to the reduction in the number of intact

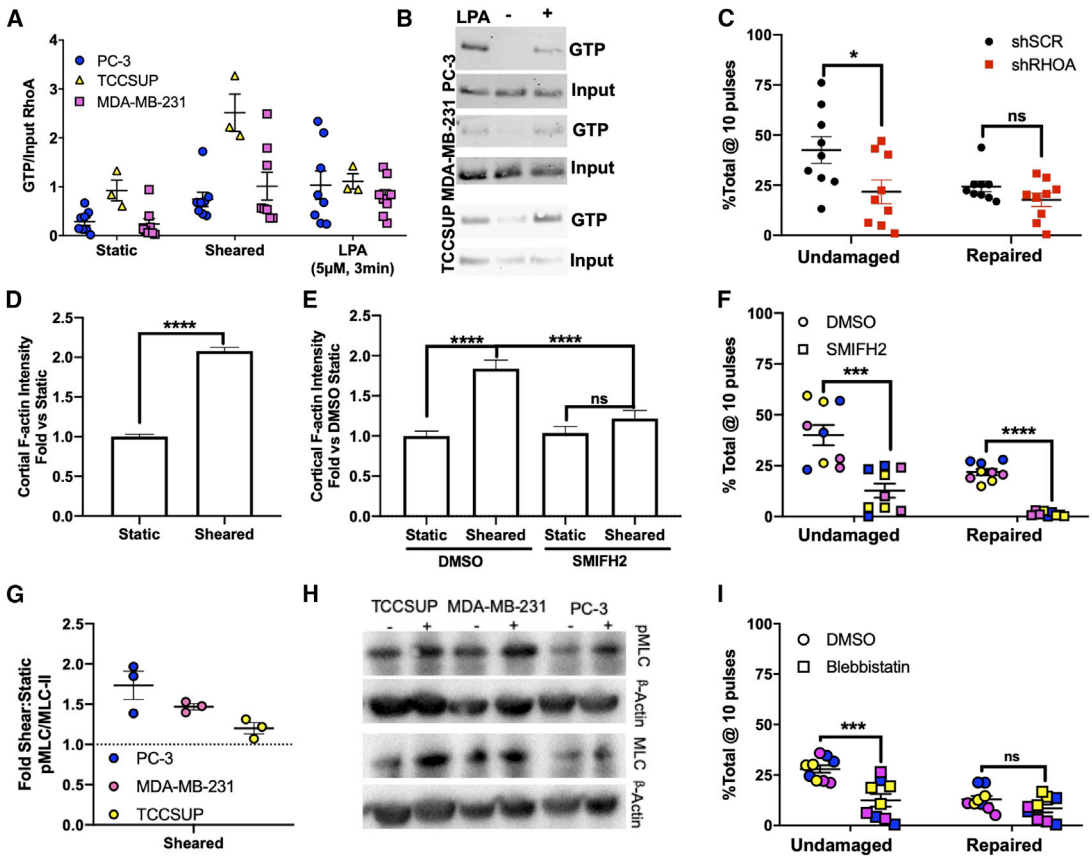

Figure 3. RhoA/Actomyosin Function Is Required for Resistance to FSS-Induced Plasma Membrane Damage

(A) RhoA activation in PC-3 (*$p < 0.05$, n = 8, Welch's t test), MDA-MB-231 (*$p < 0.05$, n = 8, Welch's t test), and TCCSUP (*$p < 0.05$, n = 3, Welch's t test) cells in suspension under static conditions (static), after two pulses of FSS (sheared), and in response to lysophosphatidic acid (LPA; positive control).

(B) Representative western blots of active RhoA from pull-down assay.

(C) Effects of 10 FSS pulses on the ability of cancer cells to resist plasma membrane damage (*$p < 0.05$, t test, n = 9) and repair damage in cells treated with control and RhoA-targeting shRNAs ($p > 0.05$, n = 9, t test).

(D) Effects of FSS pulses on cortical F-actin levels in PC-3 cells (****$p < 0.0001$, Mann-Whitney U test).

(E) Effects of SMIFH2 on F-actin levels after FSS exposure (****$p < 0.0001$, Kruskal-Wallis with Dunn's correction and two-way ANOVA).

(F) Effects of SMIFH2 on the ability for PC-3, MDA-MB-231, and TCCSUP to remain undamaged and repair plasma membrane damage after 10 pulses of FSS (****$p < 0.0001$, t test, n = 3/cell line).

(G) Analysis of pMLC from PC-3, TCCSUP, and MDA-MB-231 after two pulses of FSS ($p < 0.05$ for all cell lines, t test, n = 3/cell line).

(H) Representative blot of (G).

(I) Effects of blebbistatin on membrane damage (***$p < 0.01$, t test, n = 3/cell line) and membrane repair ($p > 0.05$, t test, n = 3/cell line) in response to FSS exposure.

Data in (D) and (E) are presented as median with 95% confidence interval (CI) error bars; all other data are presented as mean with SEM error bars. Original blots for data presented in (B) are found in Figure S8 with boxes to outline what is presented.

See also Figures S3–S5.

cancer cells lodged in the lung microcirculation. We reasoned that this effect could have been due to either destruction of blebbistatin-treated cells *en route* to the lung or an increase in their capacity to traverse the lung microvasculature. To discriminate between these possibilities, we took advantage of the expression of firefly luciferase in the cells tested; we found that the activity of cell-free luciferase correlated with the reduction in viability of the cells exposed to FSS *in vitro* (Figures S6A–S6C). By measuring the cell-free luciferase detected in the plasma of injected mice, we were able to directly quantify the number of cells destroyed during this brief exposure to the circulation. Destruction was 2-fold higher for the blebbistatin-treated samples versus their DMSO-treated counterparts (6.2% ± 0.6% versus 3.8% ± 0.6%) (Figures 4G and S6D). Although these differences in cell lodgment and destruction were statistically significant, we note that the magnitude of the change was moderate, which could be a consequence of the very brief (few minutes) period of time during which the cancer cells were exposed to the circulation.

Inhibiting Myosin II-Based FSS Resistance Delays Metastasis Onset

Because the pretreatment of cancer cells with blebbistatin led to an increase in the fraction of cells destroyed by hemodynamic

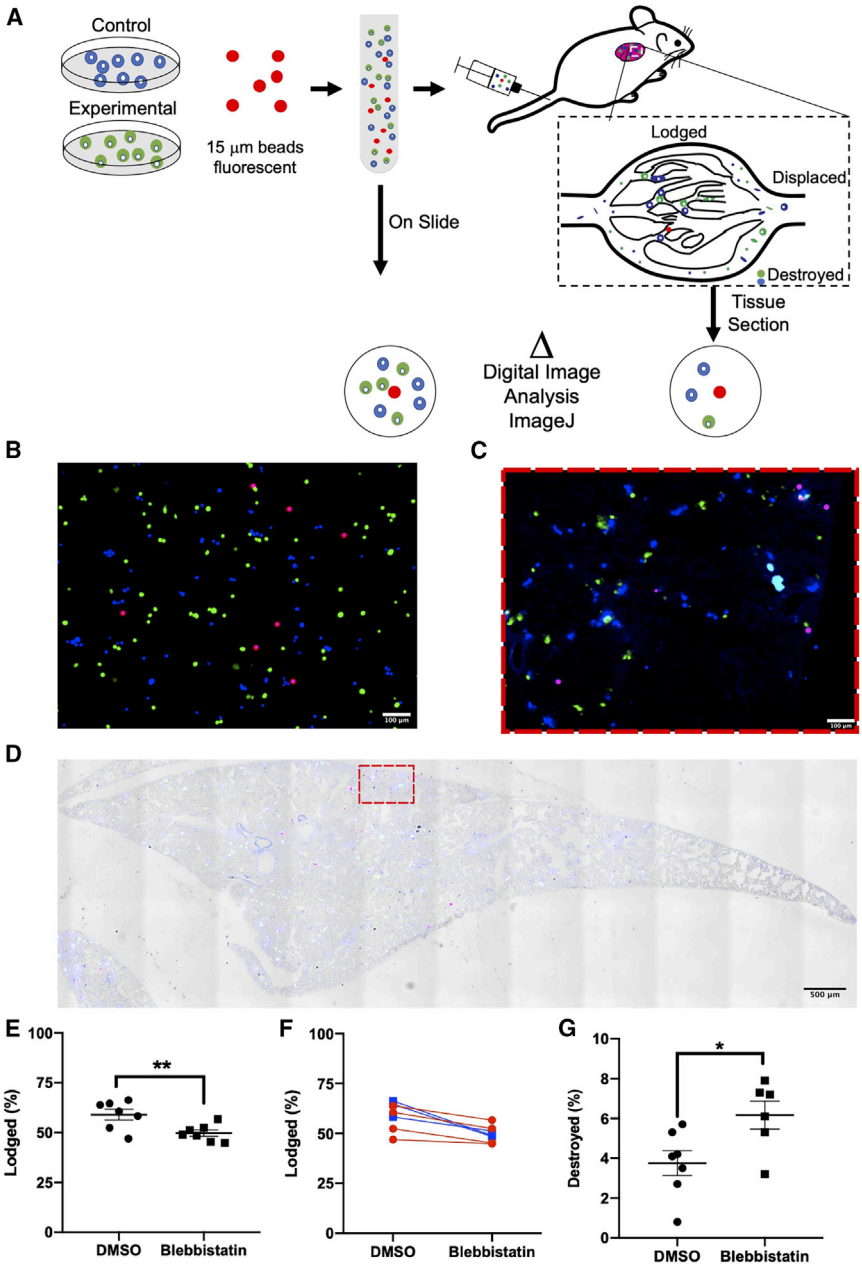

Figure 4. Myosin II Activity Is Required for the Lodgment of Intact CTCs in the Lung and Reduces Cellular Destruction Immediately following Entry into the Circulation

(A) Schematic of the experiment, with DMSO control cells (shown in blue) and blebbistatin-treated cells (shown in green) mixed with microspheres labeled red prior to injection into mouse for assessment of lodgement in the lung.

(B) Cells treated with blebbistatin are pseudocolored green and cells treated with DMSO pseudocolored blue; beads are red. Representative image of uninjected control sample ("On Slide"). Scale bar, 100 μm.

(C and D) Micrograph of whole lung section (D) and magnified portion of the lung (C) with (D) and without (C) brightfield image overlay. Colors of cells and microspheres are as depected in (B). Scale bars, 100 μm (C) and 500 μm (D).

(E–G). Quantitation of effects of blebbistatin treatment on (E and F) lodgment of intact cells (**$p < 0.01$, $n = 7$, paired t test) and (G) cell destruction (*$p < 0.05$, $n = 6$ and 7, Welch's t test). Graph of the lodgement data for each mouse, with the lines colored to group each dye condition ($p > 0.05$, two-way ANOVA, $n = 7$) (F).

Data in (E) and (G) are presented as mean with SEM error bars.

See also Figure S6 and Table S1.

forces, we wished to determine whether inhibiting this FSS resistance mechanism could delay the onset of metastasis. To evaluate this, we pretreated highly metastatic, twice *in vivo*-passaged PC-3 derivative cells with blebbistatin or DMSO (Drake et al., 2009). We then injected the cells into the tail vein of male NOD.Scid Il2gr^{null} mice and evaluated for metastasis formation by bioluminescence imaging (Figures 5A–5C). From this experiment we observed that there was a modest decrease in average tumor burden in mice injected with blebbistatin-pretreated cells (Figure 5D). Additionally, we found that there was a 17% increase in the median time for metastasis formation in the blebbistatin group (Figure 5E); this decrease in metastasis is mirrored by comparable decreases in FSS resistance *in vitro* (Figure 5F) and increased destruction *in vivo* (Figure 4G). Because blebbistatin could have implications on other aspects of metastasis, we sought to determine whether and when the effects of blebbistatin treatment were reversed following injection and the effective washout of the drug. To do this, we measured FSS resistance after a drug washout *in vitro* and found that there was a partial reversal of its effects on FSS resistance after 1 h and a near-complete reversal 3 h after blebbistatin washout (Figure 5F). Importantly, blebbistatin exposure for these experiments did not impact the clonogenic potential of these cells (Figure 5G). This suggests that the delay in metastasis formation is not due to any long-term cytotoxicity of blebbistatin but due to its ability to sensitize these cells to hemodynamic forces immediately following injection into the circulation.

CTCs Are Sensitive to Myosin II Inhibition

Our *in vivo* data presented thus far have demonstrated that by inhibiting the activity of myosin II, cancer cells are more susceptible to destruction by hemodynamic forces and that metastasis onset is delayed. However, these experiments involve pretreating cancer cells prior to injecting into mice. Thus, we wanted to test whether inhibition of myosin II can affect the survival of CTCs that arise from a tumor. To test this hypothesis, we employed an orthotopic model of metastatic prostate

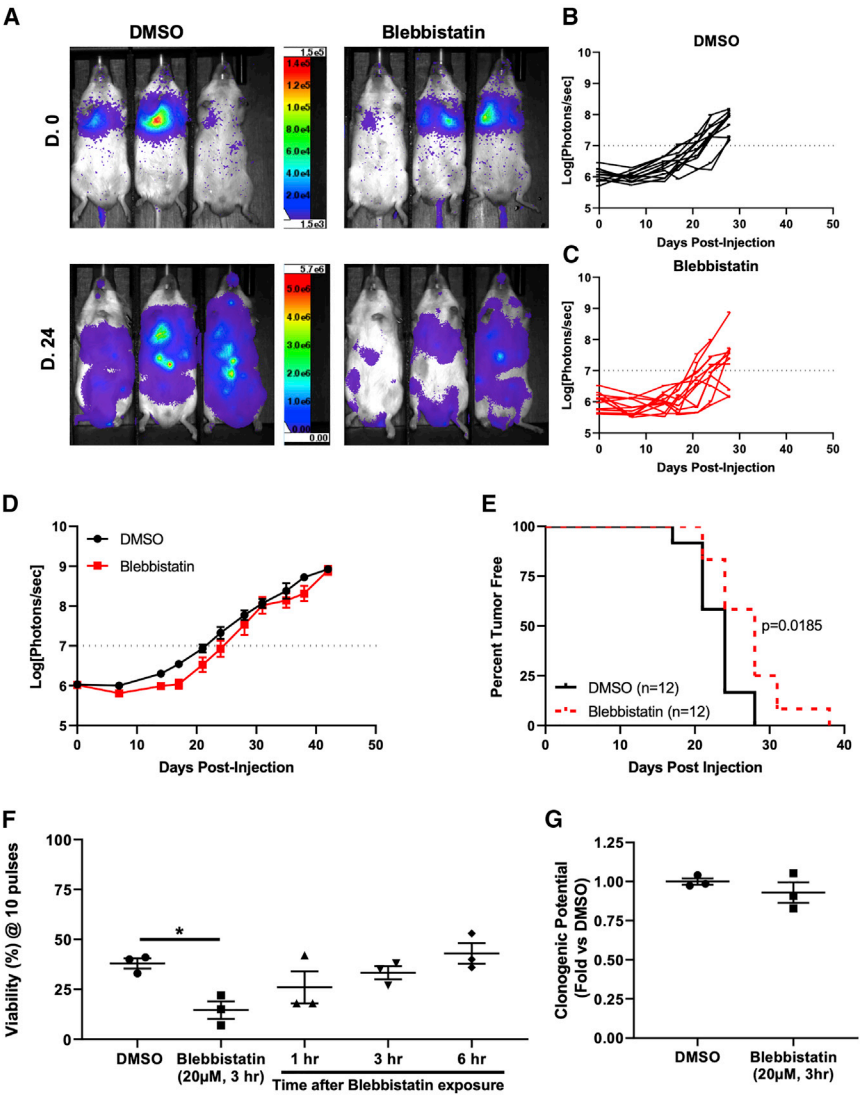

Figure 5. Pretreatment of Prostate Cancer Cells with Myosin II Inhibitor Delays Metastasis Formation

(A) Representative bioluminescence images (BLIs) on the day of injection (D.0) and 24 days after injection (D.24) for groups injected with DMSO- and blebbistatin (20 μM, 3 h)-pretreated cells.

(B) Graph of BLI data for each mouse in the DMSO group (n = 12).

(C) Graph of individual mice in the blebbistatin group (n = 12).

(D) Graph of average tumor burden (photons/s) for the two groups ($p < 0.05$, two-way ANOVA).

(E) Kaplan-Meier curve of time to metastasis formation (photon/s > 10^7) ($p = 0.0185$, log rank test).

(F) Graph of viability after 10 pulses for GS689.Li cells pretreated with DMSO or blebbistatin (20 μM, 3 h) and exposed to FSS immediately or after a washout (*$p < 0.05$, one-way ANOVA with Bonferroni correction).

(G) Clonogenic potential of GS689.Li cells pretreated with blebbistatin or DMSO ($p > 0.05$, n = 3). Data in (D), (F), and (G) are presented as mean with SEM error bars.

cancer that we had previously developed (Varzavand et al., 2016). Utilizing this model, we treated tumor-bearing mice with a single dose of blebbistatin (2.5 mg/kg) and measured CTC number in cardiac blood 3 h later (Figure 6A). Neither the overall tumor burden nor tumor growth differed between the two groups (Figure S7B). We observed a dramatic reduction in CTC number in mice treated with blebbistatin versus the vehicle control (Figures 6B and S7C). Importantly, over a range of exposures bracketing the *in vivo* exposure level, blebbistatin was not directly cytotoxic to the prostate cancer cells, indicating that the effects of blebbistatin on prostate cancer CTCs cannot be accounted for by direct toxicity (Figure S7D). Moreover, treatment of non-tumor-bearing mice with blebbistatin did not affect the number of $CD45^+$ cells detected in blood (Figure 6C), indicating that blebbistatin was not toxic to leukocytes. This suggests that the RhoA-myosin II axis promotes FSS resistance specifically in cancer cells rather than in blood cells more generally. Taken together, our data strongly indicate that targeting of the RhoA-myosin II axis could sensitize CTCs to destruction by hemodynamic forces and impede metastasis.

DISCUSSION

Cancer cells rely on the circulatory system to spread beyond the primary tumor and regional lymph nodes. This journey presents a mechanical challenge to those originating in solid organs, in part because FSS in the circulation is orders of magnitude higher than that experienced due to interstitial flow in tissues (Krog and Henry, 2018). Here we show that cancer cells actively resist FSS-induced damage to the plasma membrane via mechano-adaptation involving RhoA/actomyosin function. Our study challenges the long-held notion that CTCs are inherently fragile. Although numerous studies have shown that an appreciable fraction of CTCs are dead or in the process of dying following their isolation (Kallergi et al., 2013; Larson et al., 2004; Méhes et al., 2001; Swartz et al., 1999), the cause of death of these cells remains unclear, as they are subjected to both biological and mechanical insults (Labelle and Hynes, 2012; Strilic and Offermanns, 2017). Our data indicate that dead and dying cancer cells are highly susceptible to destruction by FSS. Therefore, the presence of dead and dying CTCs could contribute to the notion that CTCs are mechanically fragile, when in fact viable CTCs are mechanically robust. Thus, we conclude that mechanical destruction in the circulation does not contribute significantly to metastatic inefficiency, supporting a number of previous studies (Cameron et al., 2000; Fidler, 1970; Luzzi et al., 1998; Mizuno et al., 1998; Qian et al., 2009).

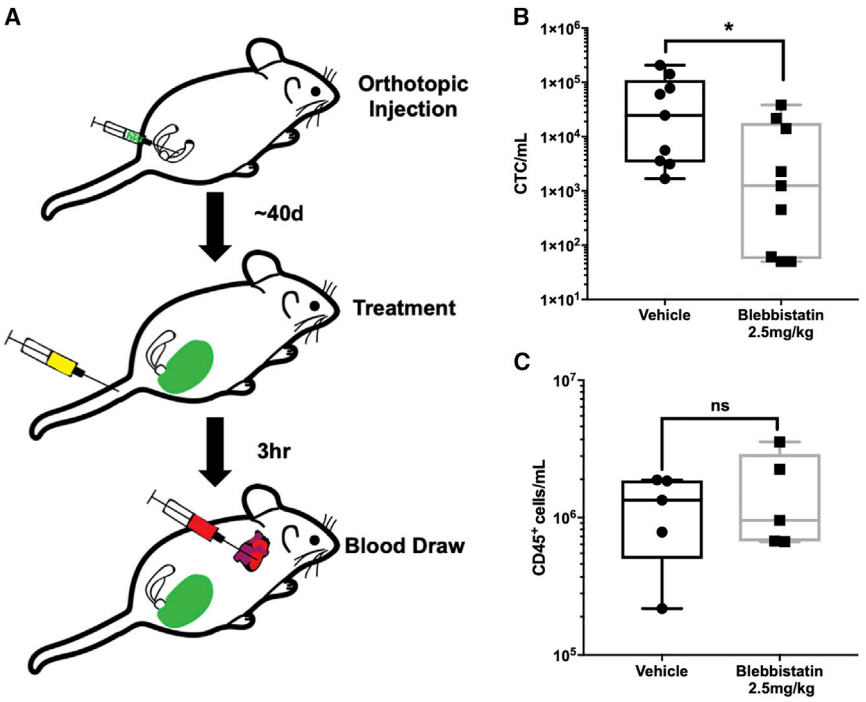

Figure 6. Myosin II Activity Is Required to Maintain Steady-State Levels of CTCs

(A) Schematic of the experiment, with orthotopic tumor cell injection, blebbistatin treatment at ~40 days, and blood draw to test CTC number 3 h later.

(B) Effects of blebbistatin treatment on CTC number (~1,200 versus ~25,000 CTCs/mL) (*$p < 0.05$, n = 9/group, Mann-Whitney U test).

(C) Effects of blebbistatin treatment on $CD45^+$ cells (1.3×10^6 versus 9.5×10^5) ($p > 0.05$, n = 5/group, Mann-Whitney U test). Data are presented as min to max box and whisker plot with the median.

See also Figure S7.

The precise magnitude and duration of FSS and other hemodynamic forces that CTCs experience in the circulation are not entirely clear (Krog and Henry, 2018). The best available evidence indicates that the periods during which CTCs circulate freely last only a few seconds and are interspersed between much longer periods during which CTCs are trapped in the microcirculation due to size restriction. However, CTCs vary in size, and some may be less prone to lodgment in the microcirculation (Chen et al., 2015). Passage through the heart may expose CTCs to brief high-magnitude FSS, most similar to that used in our *in vitro* model. Using this model, we showed that the ability of cells to resist plasma membrane damage, as opposed to elevated repair capacity, most consistently distinguished cancer cell lines (bladder, breast, and prostate) from their non-transformed epithelial counterparts. In PC-3 prostate cancer cells, we observed that exposure to FSS produced small (<12 nm) holes in the plasma membrane. These small holes may be rapidly repaired via tensional forces in the plasma membrane (Jimenez and Perez, 2015). It is possible that RhoA/actomyosin function protects CTCs from damage by hemodynamic forces as shown here, but that this activity is modulated dynamically as CTCs traverse the microcirculation, with cells that are less stiff more readily passing through narrow capillaries (Nyberg et al., 2016). In our studies, the reduced lodgment of blebbistatin-treated cells in the lung microcirculation was not evenly balanced by the observed increase in destruction, suggesting that some of these potentially more compliant blebbistatin-treated cells may have avoided lodgment in the microcirculation. The ability of cancer cells to navigate confined pores in the extracellular matrix during invasion or capillary constrictions following arrest in the microcirculation, steps in metastasis occurring just before or just after CTCs are freely circulating, may be facilitated by a softer, more compliant mechanotype (Mosier et al., 2019; Nyberg et al., 2018; Raman et al., 2013; Rianna et al., 2020; Swaminathan et al., 2011; Xu et al., 2012). Thus, rapid mechano-adaptation of cancer cells in the circulation may confer a survival advantage and allow for dynamic regulation of their mechanical properties as they encounter diverse mechanical challenges in their metastatic journey.

We show that FSS resistance is a phenotype in cancer cells isolated directly from primary tumors. It is not an artifact of cell culture, nor the product of metastatic selection. Our previous study indicated that FSS resistance is conferred by various transforming oncogenes, such as *ras*, *PI3K*, and *myc*. Although detailed mechanisms remain elusive, plausible mechanisms linking *ras* with RhoA activity had been previously reported (Chen et al., 2003). Our finding that exposure to FSS activates RhoA indicates that the development of resistance to FSS is a mechano-adaptive response. Previously, we found that exposure to FSS results in cell stiffening (Chivukula et al., 2015), which likely reflects activation of RhoA-dependent contractility. In addition to the activation of myosin II, we show that FSS triggers a formin-dependent increase in cortical F-actin, which may also contribute to increased cell stiffness (Cartagena-Rivera et al., 2016; Fritzsche et al., 2016). Our findings show that formin activity is more important for FSS resistance than Arp2/3 activity. We do not yet know exactly what triggers RhoA activation in response to the mechanical stimulus of FSS. Our demonstration that extracellular calcium is essential for FSS resistance in cancer cells (Barnes et al., 2012) suggests that calcium influx, through either small membrane disruptions that we detect or possibly a mechanosensitive ion channel, activates RhoA or triggers myosin II contractility directly. Alternatively, mechano-activation of formins associated with the plasma membrane, including some whose activation is calcium dependent, may constitute the relevant mechanosensor driving FSS resistance (Harris et al., 2016; Hegsted et al., 2017; Lessey et al., 2012). Although we find that the RhoA/actomyosin axes are important for FSS resistance, our efforts to genetically or pharmacologically inhibit these pathways did not completely ablate FSS resistance. Cell stiffness is a complex phenotype involving cytoskeletal structure and force generation, as well as the properties of the glycocalyx, composition of the plasma

membrane, osmotic state, and nuclear structure and stiffness, with the latter having already been implicated in FSS resistance (Fels et al., 2014; Mitchell et al., 2015). Thus, other mechanisms are likely to modulate FSS resistance in cancer cells.

Our demonstration that a short-term blockade of myosin II activity leads to an increase in the destruction of CTCs and a delay in metastatic colonization has interesting implications. We sought to temporally restrict the effects of myosin II inhibition to a short window of time (3–6 h) after injection to test the role of FSS resistance in metastatic colonization by treating cells with a non-toxic exposure to blebbistatin *in vitro* and then washing out the drug prior to systemic injection of the cells into mice. We found that blebbistatin treatment in this manner reduced the onset of metastatic colonization assessed weeks following injection. Although we favor the interpretation that this results from decreased short-term survival of CTCs immediately post-injection, we cannot rule out the possibility that the short-term treatment with the drug initiated changes in gene expression that resulted in effects on later steps of metastasis. Indeed, exposure to FSS is known to induce changes in gene expression in many cell types, including cancer cells, which could contribute to metastatic behavior (Lee et al., 2017). This also raises the interesting possibility that exposure to FSS "primes" cells for subsequent metastatic behavior by activating RhoA/actomyosin function. Finally, whereas acute treatment with blebbistatin reduces FSS resistance *in vitro* and short-term survival of CTCs *in vivo*, with a reduction of over an order of magnitude within 3 h of treatment, this treatment did not affect the number of $CD45^+$ leukocytes. These outcomes suggest that myosin II-mediated FSS resistance is specific for cancer cells, and thus this might constitute a therapeutic opportunity. Intervening in the steps of metastatic dissemination for therapeutic benefit is regarded as challenging because dissemination may occur before cancer diagnosis (Friberg and Nyström, 2015). However, metastatic seeding is likely an ongoing process in cancer patients (Kim et al., 2009) and during surgical and diagnostic procedures, CTCs may be liberated and could be targeted at that time (Martin et al., 2017). Our results suggest the possibility that targeting FSS resistance may be an effective anti-metastatic therapy. Moreover, because the activation of RhoA-myosin II has been implicated in other aspects of cellular behavior that could promote metastatic colonization, e.g., extravasation, cell invasion, and cell survival (Haga and Ridley, 2016), the anti-metastatic benefits of inhibiting this pathway may be pleiotropic.

STAR★METHODS

Detailed methods are provided in the online version of this paper and include the following:

SUPPLEMENTAL INFORMATION

Supplemental Information can be found online at https://doi.org/10.1016/j.celrep.2020.02.080.

ACKNOWLEDGMENTS

We would like to thank Justin Fishbaugh and Dr. Chantal Allamargot for technical assistance with flow cytometry and microscopy, respectively, and Drs. Christine Blaumueller, Kevin Campbell, Frank Solomon, and Dan Welch for helpful comments on the manuscript. Human tumor specimens were obtained through the University of Iowa Melanoma, Skin & Ocular Repository (MaST), an Institutional Review Board-approved biospecimen repository. This project was supported by the NIH (grants R21 CA179981 and R21 CA196202 to M.D.H.), the National Science Foundation (grant BMMB-1906165 to A.C.R.), and the University of California Cancer Research Coordinating Committee (grant CRR-18-52690 to A.C.R.). D.L.M. was supported by Pharmacological Sciences Training grant 2T32-GM0677954-14. Core facilities at the University of Iowa were supported by grant P30 CA086862 to the Holden Comprehensive Cancer Center. This research was also supported by a kind gift from the Sato Metastasis Research Fund.

AUTHOR CONTRIBUTIONS

Conceptualization, D.L.M., B.L.K., and M.D.H.; Analysis, D.L.M., B.L.K., L.Z., T.-H.K., P.B., A.C.R., and M.D.H.; Investigation, D.L.M., B.L.K., L.Z., T.-H.K., S.W.-P., G.B., and L.R.; Methodology, D.L.M., B.L.K., T.-H.K., C.S.S., A.C.R., and M.D.H.; Project Administration, M.D.H.; Resources, M.V., M.M., and C.S.S.; Writing – Original Draft, D.L.M. and M.D.H.; Writing – Review & Editing, all authors.

DECLARATION OF INTERESTS

M.D.H. is president, co-founder, and shareholder of SynderBio, Inc.

Received: October 3, 2019
Revised: January 31, 2020
Accepted: February 20, 2020
Published: March 17, 2020

REFERENCES

Alexander, M.S., O'Leary, B.R., Moose, D., Du, J., Henry, M.D., and Cullen, J.J. (2018). A model for the detection of pancreatic ductal adenocarcinoma circulating tumor cells. J. Biol. Methods *5*, e97.

Amano, M., Ito, M., Kimura, K., Fukata, Y., Chihara, K., Nakano, T., Matsuura, Y., and Kaibuchi, K. (1996). Phosphorylation and activation of myosin by Rho-associated kinase (Rho-kinase). J. Biol. Chem. *271*, 20246–20249.

Antiga, L., and Steinman, D.A. (2009). Rethinking turbulence in blood. Biorheology *46*, 77–81.

Barnes, J.M., Nauseef, J.T., and Henry, M.D. (2012). Resistance to fluid shear stress is a conserved biophysical property of malignant cells. PLoS ONE *7*, e50973.

Buchakjian, M.R., Merritt, N.M., Moose, D.L., Dupuy, A.J., Tanas, M.R., and Henry, M.D. (2017). A Trp53fl/flPtenfl/fl mouse model of undifferentiated pleomorphic sarcoma mediated by adeno-Cre injection and in vivo bioluminescence imaging. PLoS ONE *12*, e0183469.

Cameron, M.D., Schmidt, E.E., Kerkvliet, N., Nadkarni, K.V., Morris, V.L., Groom, A.C., Chambers, A.F., and MacDonald, I.C. (2000). Temporal progression of metastasis in lung: cell survival, dormancy, and location dependence of metastatic inefficiency. Cancer Res. *60*, 2541–2546.

Cartagena-Rivera, A.X., Logue, J.S., Waterman, C.M., and Chadwick, R.S. (2016). Actomyosin Cortical Mechanical Properties in Nonadherent Cells Determined by Atomic Force Microscopy. Biophys. J. *110*, 2528–2539.

Chen, J.C., Zhuang, S., Nguyen, T.H., Boss, G.R., and Pilz, R.B. (2003). Oncogenic Ras leads to Rho activation by activating the mitogen-activated protein kinase pathway and decreasing Rho-GTPase-activating protein activity. J. Biol. Chem. *278*, 2807–2818.

Chen, Z., Trotman, L.C., Shaffer, D., Lin, H.K., Dotan, Z.A., Niki, M., Koutcher, J.A., Scher, H.I., Ludwig, T., Gerald, W., et al. (2005). Crucial role of p53-dependent cellular senescence in suppression of Pten-deficient tumorigenesis. Nature *436*, 725–730.

Chen, J.F., Ho, H., Lichterman, J., Lu, Y.T., Zhang, Y., Garcia, M.A., Chen, S.F., Liang, A.J., Hodara, E., Zhau, H.E., et al. (2015). Subclassification of prostate cancer circulating tumor cells by nuclear size reveals very small nuclear circulating tumor cells in patients with visceral metastases. Cancer *121*, 3240–3251.

Chivukula, V.K., Krog, B.L., Nauseef, J.T., Henry, M.D., and Vigmostad, S.C. (2015). Alterations in cancer cell mechanical properties after fluid shear stress exposure: a micropipette aspiration study. Cell Health Cytoskelet. *7*, 25–35.

Cui, X., Dean, D., Ruggeri, Z.M., and Boland, T. (2010). Cell damage evaluation of thermal inkjet printed Chinese hamster ovary cells. Biotechnol. Bioeng. *106*, 963–969.

Dixon, J.B., Greiner, S.T., Gashev, A.A., Cote, G.L., Moore, J.E., and Zawieja, D.C. (2006). Lymph flow, shear stress, and lymphocyte velocity in rat mesenteric prenodal lymphatics. Microcirculation *13*, 597–610.

Drake, J.M., Gabriel, C.L., and Henry, M.D. (2005). Assessing tumor growth and distribution in a model of prostate cancer metastasis using bioluminescence imaging. Clin Exp Metastasis *22*, 674–684.

Drake, J.M., Strohbehn, G., Bair, T.B., Moreland, J.G., and Henry, M.D. (2009). ZEB1 enhances transendothelial migration and represses the epithelial phenotype of prostate cancer cells. Mol. Biol. Cell *20*, 2207–2217.

Egan, K., Cooke, N., and Kenny, D. (2014). Living in shear: platelets protect cancer cells from shear induced damage. Clin. Exp. Metastasis *31*, 697–704.

Fels, J., Jeggle, P., Liashkovich, I., Peters, W., and Oberleithner, H. (2014). Nanomechanics of vascular endothelium. Cell Tissue Res. *355*, 727–737.

Fidler, I.J. (1970). Metastasis: quantitative analysis of distribution and fate of tumor emboli labeled with 125 I-5-iodo-2′-deoxyuridine. J. Natl. Cancer Inst. *45*, 773–782.

Friberg, S., and Nyström, A. (2015). Cancer Metastases: Early Dissemination and Late Recurrences. Cancer Growth Metastasis *8*, 43–49.

Fritzsche, M., Erlenkämper, C., Moeendarbary, E., Charras, G., and Kruse, K. (2016). Actin kinetics shapes cortical network structure and mechanics. Sci. Adv. *2*, e1501337.

Furlow, P.W., Zhang, S., Soong, T.D., Halberg, N., Goodarzi, H., Mangrum, C., Wu, Y.G., Elemento, O., and Tavazoie, S.F. (2015). Mechanosensitive pannexin-1 channels mediate microvascular metastatic cell survival. Nat. Cell Biol. *17*, 943–952.

Haga, R.B., and Ridley, A.J. (2016). Rho GTPases: Regulation and roles in cancer cell biology. Small GTPases *7*, 207–221.

Harris, A.R., Jreij, P., and Fletcher, D.A. (2016). Mechanotransduction by the Actin Cytoskeleton: Converting Mechanical Stimuli into Biochemical Signals. Annu. Rev. Biophys. *47*, 617–631.

Hegsted, A., Yingling, C.V., and Pruyne, D. (2017). Inverted formins: A subfamily of atypical formins. Cytoskeleton (Hoboken) *74*, 405–419.

Jégou, A., Carlier, M.F., and Romet-Lemonne, G. (2013). Formin mDia1 senses and generates mechanical forces on actin filaments. Nat. Commun. *4*, 1883.

Jimenez, A.J., and Perez, F. (2015). Physico-chemical and biological considerations for membrane wound evolution and repair in animal cells. Semin. Cell Dev. Biol. *45*, 2–9.

Kallergi, G., Konstantinidis, G., Markomanolaki, H., Papadaki, M.A., Mavroudis, D., Stournaras, C., Georgoulias, V., and Agelaki, S. (2013). Apoptotic circulating tumor cells in early and metastatic breast cancer patients. Mol. Cancer Ther. *12*, 1886–1895.

Kim, M.Y., Oskarsson, T., Acharyya, S., Nguyen, D.X., Zhang, X.H.F., Norton, L., and Massagué, J. (2009). Tumor self-seeding by circulating cancer cells. Cell *139*, 1315–1326.

Kimura, K., Ito, M., Amano, M., Chihara, K., Fukata, Y., Nakafuku, M., Yamamori, B., Feng, J., Nakano, T., Okawa, K., et al. (1996). Regulation of myosin phosphatase by Rho and Rho-associated kinase (Rho-kinase). Science *273*, 245–248.

Krog, B.L., and Henry, M.D. (2018). Biomechanics of the circulating tumor cell microenvironment. In Biomechanics in Oncology, C. Dong, N. Zahir, and K. Konstantopoulos, eds. (Springer International Publishing), pp. 209–233.

Kubota, H., Miyazaki, M., Ogawa, T., Shimozawa, T., Kinosita, K., Jr., and Ishiwata, S. (2017). Biphasic Effect of Profilin Impacts the Formin mDia1 Force-Sensing Mechanism in Actin Polymerization. Biophys. J. *113*, 461–471.

Labelle, M., and Hynes, R.O. (2012). The initial hours of metastasis: the importance of cooperative host-tumor cell interactions during hematogenous dissemination. Cancer Discov. *2*, 1091–1099.

Larson, C.J., Moreno, J.G., Pienta, K.J., Gross, S., Repollet, M., O'hara, S.M., Russell, T., and Terstappen, L.W. (2004). Apoptosis of circulating tumor cells in prostate cancer patients. Cytometry A *62*, 46–53.

Lee, H.J., Diaz, M.F., Price, K.M., Ozuna, J.A., Zhang, S., Sevick-Muraca, E.M., Hagan, J.P., and Wenzel, P.L. (2017). Fluid shear stress activates YAP1 to promote cancer cell motility. Nat. Commun. *8*, 14122.

Lessey, E.C., Guilluy, C., and Burridge, K. (2012). From mechanical force to RhoA activation. Biochemistry *51*, 7420–7432.

Luzzi, K.J., MacDonald, I.C., Schmidt, E.E., Kerkvliet, N., Morris, V.L., Chambers, A.F., and Groom, A.C. (1998). Multistep nature of metastatic inefficiency: dormancy of solitary cells after successful extravasation and limited survival of early micrometastases. Am. J. Pathol. *153*, 865–873.

Martin, O.A., Anderson, R.L., Narayan, K., and MacManus, M.P. (2017). Does the mobilization of circulating tumour cells during cancer therapy cause metastasis? Nat. Rev. Clin. Oncol. *14*, 32–44.

Méhes, G., Witt, A., Kubista, E., and Ambros, P.F. (2001). Circulating breast cancer cells are frequently apoptotic. Am. J. Pathol. *159*, 17–20.

Mitchell, M.J., Denais, C., Chan, M.F., Wang, Z., Lammerding, J., and King, M.R. (2015). Lamin A/C deficiency reduces circulating tumor cell resistance to fluid shear stress. Am. J. Physiol. Cell Physiol. *309*, C736–C746.

Mizuno, N., Kato, Y., Shirota, K., Izumi, Y., Irimura, T., Harashima, H., Kiwada, H., Motoji, N., Shigematsu, A., and Sugiyama, Y. (1998). Mechanism of initial distribution of blood-borne colon carcinoma cells in the liver. J. Hepatol. *28*, 878–885.

Mohandas, N., and Evans, E. (1994). Mechanical properties of the red cell membrane in relation to molecular structure and genetic defects. Annu. Rev. Biophys. Biomol. Struct. *23*, 787–818.

Mosier, J.A., Rahman-Zaman, A., Zanotelli, M.R., VanderBurgh, J.A., Bordeleau, F., Hoffman, B.D., and Reinhart-King, C.A. (2019). Extent of Cell Confinement in Microtracks Affects Speed and Results in Differential Matrix Strains. Biophys. J. *117*, 1692–1701.

Nyberg, K.D., Scott, M.B., Bruce, S.L., Gopinath, A.B., Bikos, D., Mason, T.G., Kim, J.W., Choi, H.S., and Rowat, A.C. (2016). The physical origins of transit time measurements for rapid, single cell mechanotyping. Lab Chip *16*, 3330–3339.

Nyberg, K.D., Bruce, S.L., Nguyen, A.V., Chan, C.K., Gill, N.K., Kim, T.H., Sloan, E.K., and Rowat, A.C. (2018). Predicting cancer cell invasion by single-cell physical phenotyping. Integr. Biol. *10*, 218–231.

Popel, A.S., and Johnson, P.C. (2005). Microcirculation and Hemorheology. Annu. Rev. Fluid Mech. *37*, 43–69.

Qian, B., Deng, Y., Im, J.H., Muschel, R.J., Zou, Y., Li, J., Lang, R.A., and Pollard, J.W. (2009). A distinct macrophage population mediates metastatic breast cancer cell extravasation, establishment and growth. PLoS ONE *4*, e6562.

Raman, P.S., Paul, C.D., Stroka, K.M., and Konstantopoulos, K. (2013). Probing cell traction forces in confined microenvironments. Lab Chip *13*, 4599–4607.

Rianna, C., Radmacher, M., and Kumar, S. (2020). Direct evidence that tumor cells soften when navigating confined spaces. Mol. Biol. Cell. Published online January 29, 2020. https://doi.org/10.1091/mbc.E19-10-0588.

Ridley, A.J., and Hall, A. (1992). The small GTP-binding protein rho regulates the assembly of focal adhesions and actin stress fibers in response to growth factors. Cell *70*, 389–399.

Risca, V.I., Wang, E.B., Chaudhuri, O., Chia, J.J., Geissler, P.L., and Fletcher, D.A. (2012). Actin filament curvature biases branching direction. Proc. Natl. Acad. Sci. USA *109*, 2913–2918.

Rueden, C.T., Schindelin, J., Hiner, M.C., DeZonia, B.E., Walter, A.E., Arena, E.T., and Eliceiri, K.W. (2017). ImageJ2: ImageJ for the next generation of scientific image data. BMC Bioinformatics *18*, 529.

Spiering, D., and Hodgson, L. (2011). Dynamics of the Rho-family small GTPases in actin regulation and motility. Cell Adhes. Migr. *5*, 170–180.

Strilic, B., and Offermanns, S. (2017). Intravascular Survival and Extravasation of Tumor Cells. Cancer Cell *32*, 282–293.

Strony, J., Beaudoin, A., Brands, D., and Adelman, B. (1993). Analysis of shear stress and hemodynamic factors in a model of coronary artery stenosis and thrombosis. Am. J. Physiol. *265*, H1787–H1796.

Svensson, R.U., Haverkamp, J.M., Thedens, D.R., Cohen, M.B., Ratliff, T.L., and Henry, M.D. (2011). Slow disease progression in a C57BL/6 pten-deficient mouse model of prostate cancer. Am. J. Pathol. *179*, 502–512.

Swaminathan, V., Mythreye, K., O'Brien, E.T., Berchuck, A., Blobe, G.C., and Superfine, R. (2011). Mechanical stiffness grades metastatic potential in patient tumor cells and in cancer cell lines. Cancer Res. *71*, 5075–5080.

Swartz, M.A., Kristensen, C.A., Melder, R.J., Roberge, S., Calautti, E., Fukumura, D., and Jain, R.K. (1999). Cells shed from tumours show reduced clonogenicity, resistance to apoptosis, and in vivo tumorigenicity. Br. J. Cancer *81*, 756–759.

Triantafillu, U.L., Park, S., Klaassen, N.L., Raddatz, A.D., and Kim, Y. (2017). Fluid shear stress induces cancer stem cell-like phenotype in MCF7 breast cancer cell line without inducing epithelial to mesenchymal transition. Int. J. Oncol. *50*, 993–1001.

Vácha, J. (1975). Blood volume in inbred strain BALB/c, CBA/J and C57BL/10 mice determined by means of 59Fe-labelled red cells and 59Fe bound to transferrin. Physiol. Bohemoslov. *24*, 413–419.

Varzavand, A., Hacker, W., Ma, D., Gibson-Corley, K., Hawayek, M., Tayh, O.J., Brown, J.A., Henry, M.D., and Stipp, C.S. (2016). $\alpha 3\beta 1$ Integrin Suppresses Prostate Cancer Metastasis via Regulation of the Hippo Pathway. Cancer Res. *76*, 6577–6587.

Vennin, C., Chin, V.T., Warren, S.C., Lucas, M.C., Herrmann, D., Magenau, A., Melenec, P., Walters, S.N., Del Monte-Nieto, G., Conway, J.R.W., et al.; Australian Pancreatic Cancer Genome Initiative (APGI) (2017). Transient tissue priming via ROCK inhibition uncouples pancreatic cancer progression, sensitivity to chemotherapy, and metastasis. Sci. Transl. Med. *9*, eaai8504.

Weiss, L. (1990). Metastatic inefficiency. Adv. Cancer Res. *54*, 159–211.

Wirtz, D., Konstantopoulos, K., and Searson, P.C. (2011). The physics of cancer: the role of physical interactions and mechanical forces in metastasis. Nat. Rev. Cancer *11*, 512–522.

Xu, W., Mezencev, R., Kim, B., Wang, L., McDonald, J., and Sulchek, T. (2012). Cell stiffness is a biomarker of the metastatic potential of ovarian cancer cells. PLoS ONE *7*, e46609.

Zeidman, I., McCutcheon, M., and Coman, D.R. (1950). Factors affecting the number of tumor metastases; experiments with a transplantable mouse tumor. Cancer Res. *10*, 357–359.

STAR★METHODS

KEY RESOURCES TABLE

REAGENT or RESOURCE	SOURCE	IDENTIFIER
Antibodies		
RhoA	Cytoskeleton, Inc.	Cat# ARH04; RRID: AB_2728698
Myosin Light Chain II	Cell Signaling	Cat# 3672; RRID: AB_10692513
Phospho-Myosin Light Chain II	Cell Signaling	Cat# 3671; RRID: AB_330248
β-Actin	Sigma	Cat# A1978; RRID: AB_476692
β-tubulin	Developmental Studies Hybridoma Bank	Cat# 6G7; RRID: AB_528497
Goat-anti-mouse	Rockland	Cat# 610-731-124; RRID: AB_220145
Goat anti-mouse	Jackson Labs	Cat# 715-036-151; RRID: AB_2340774
CD45	BioLegend	Cat# 103110; RRID: AB_312975
Bacterial and Virus Strains		
BL21(DE3)pLysS	Life Technologies	C6060-03
DH5 alpha	Life Technologies	18265-017
Biological Samples		
PDX Sample 1-metastatic	UI Tissue Procurement Core	N/A
PDX Sample 4-metastatic	UI Tissue Procurement Core	N/A
PDX Sample 8-primary	UI Tissue Procurement Core	N/A
PDX Sample 16-metastatic	UI Tissue Procurement Core	N/A
PDX Sample 17-primary	UI Tissue Procurement Core	N/A
PDX Sample 19-primary	UI Tissue Procurement Core	N/A
Chemicals, Peptides, and Recombinant Proteins		
(-)-Blebbistatin	Selleckchem	S7099
Fasudil (HA-1077)	Selleckchem	S1573
Staurosporine	Selleckchem	S7099
ML-7	Sigma-Aldrich	I2764
CK-666	Millipore Sigma	182515
SMIFH2	Millipore Sigma	344092
Hoechst 33342	Invitrogen	H1399
Hoechst 33258	Thermo Fisher	H3569
Propidium Iodide	Invitrogen	P1304MP
K^+ D-Luciferin	GoldBio	LUCK-1G
Ionomycin	Sigma-Aldrich	I9657
DRAQ5	ThermoFisher	62251
Lysophosphatidic acid	Sigma	L7260
Critical Commercial Assays		
APC Annexin V	BioLegend	640920
Cell Titer Blue	Promega	G8080
Phalloidin-AlexaFluor488	ThermoFisher	A12379
Experimental Models: Cell Lines		
PC-3	ATCC	CRL-1435
MDA-MB-231	ATCC	HTB-26
TCCSUP	ATCC	HTB-5
Primary Bladder Epithelial Cells	ATCC	PCS-420-010
MCF-10A	ATCC	CRL-10317

(*Continued on next page*)

Continued

REAGENT or RESOURCE	SOURCE	IDENTIFIER
PrEC-LH	Dr. William Hahn	PMID: 15604246
GS689.Li	Our Lab	(Drake et al., 2009)
Experimental Models: Organisms/Strains		
NSG.Cg-*Prkdc*^{scid}*Il2rgtm1Wjl*/SzJ	The Jackson Laboratory	005557
NOD-*Prkdc*^{em26Cd52}*Il2rg*^{em26Cd22}/NjuCrl	Charles River	572
NCI BALB/cAnNcr	Charles River	555
C57BL/6J-Tyr^{c-2J}/J ROSA26LSL-Luc;Pten$^{fl/fl}$;Pb-Cre4^{+}	Our Lab	(Svensson et al., 2011)
B6.129P2-Trp53^{tm1Brn}/J	The Jackson Laboratory	008462
Recombinant DNA		
pLKO.1_RhoA shRNA	Sigma-Aldrich	TRCN0000047712
pLKO.1_RhoA shRNA	Sigma-Aldrich	TRCN0000047711
pLKO.1_SCR shRNA	Sigma-Aldrich	SHC001
pQCXIN-luc	Our Lab	(Drake et al., 2005)
pGEX_RBD	Dr. Kris DeMali	(Varzavand et al., 2016)
pQCXIP-EGFP	Dr. Christopher Stipp	(Varzavand et al., 2016)
Other		
FITC Dextran (3000 MW)	LifeTechnologies	D1821
FITC Dextran (10000 MW)	LifeTechnologies	D3305
FITC Dextran (40000 MW)	LifeTechnologies	D1844
FITC Dextran (70000 MW)	LifeTechnologies	D1823
15μm Scarlet Microspheres	Invitrogen	F8843
2μm YG microspheres	Polyscience	17155-2
PHD1000 Syringe Pump	Harvard Apparatus	703006

LEAD CONTACT AND MATERIALS AVAILABILITY

Further information and requests for resources and reagents should be directed to and will be fulfilled by the Lead Contact, Michael Henry (michael-henry@uiowa.edu). All unique/stable reagents generated in this study are available from the Lead Contact with a completed Materials Transfer Agreement.

EXPERIMENTAL MODEL AND SUBJECT DETAILS

Cell lines

All cell lines were cultured according to protocols provided by the suppliers. Cancer cell lines were obtained from ATCC. Primary bladder epithelial cells were acquired from Lonza. The non-transformed prostate epithelial cell line PrEC LH was acquired from Dr. William Hahn (Dana Farber Cancer Institute). The GS689.Li cell line was derived from the human prostate cancer cell line PC-3 that were twice selected *in vivo* for increased metastatic potential (Drake et al., 2009). The identity of this cell line as a derivative of PC-3 cells was validated by short tandem repeat (STR) analysis (IDEXX). Cells of both the PC-3 and GS689.Li lines were cultured in DMEM/F12 (GIBCO) supplemented with 10% FBS (Atlanta Biologicals, S11150) and 1X NEAA (Invitrogen). The breast cancer line MDA-MB-231, 293FT, and human epithelial kidney line HEK293T were cultured in DMEM with 10% FBS, and 1X NEAA. PrEC-LH cells were cultured in prostate epithelial cell growth medium (Lonza, CC-3166), primary bladder epithelial cells were cultured in prostate epithelial basal medium (ATCC, PCS-440-030) using the corneal epithelial growth kit (ATCC, PCS-700-040), and cells of the non-tumorigenc breast cancer cell line MCF-10A were cultured in DMEM/F12 with 5% horse serum (Invitrogen, 16050), 20 ng/mL EGF (Sino Biological, 10605HNAE250), 0.5 μg/mL hydrocortisone (ACROS, 352450010), 10 μg/mL insulin (Sigma, 91077C), and 1x Pen/Strep (Invitrogen, 15070). PC-3, GS689.Li, and MDA-MB-231 cells were transfected with an integrating retrovirus that encodes the firefly luciferase gene, which was generated by transfecting GP2-239 cells with VSV-G and pQXCIN vector containing the luciferase gene using the Polyfect reagent (QIAGEN). RhoA knockdown lentivirus and its control were generated by transfecting 293FT cells with VSVG and the PLKO.1 vector, with the latter of containing a short hairpin RNA (shRNA) targeting either RhoA or a non-target sequence (Sigma), using the Polyfect reagent (QIAGEN). The cells were selected for antibiotic resistance 2 days after transduction, and knockdown was evaluated by western blot analysis.

Animal models

All procedures were approved by the University of Iowa Animal Care and Use Committee (protocol #'s 1302028, 4121221, 5121574).

Genetically engineered mouse model of prostate cancer

The C57BL/6J-Try^{c-2J}/J ROSA26-LSL-Luc;Pbsn-cre;Pten$^{fl/fl}$ mice were generated as described previously (Svensson et al., 2011). The C57BL/6J-Try^{c-2J}/J ROSA26-LSL-Luc; Pbsn-cre; Pten$^{fl/fl}$; Trp53$^{fl/fl}$ mice were generated by breeding Pten knockout mice with B6.129P2-Trp53^{tm1Brn}/J counterparts (Jackson Laboratory) and backcrossing progeny for 6 generations onto the C57BL/6J-Tyr^{c-2J} background (Buchakjian et al., 2017). When mice of the test generation were 25 weeks of age, prostate tissue was collected from those with Cre-activated luciferase that were homozygous for either the wild-type allele, floxed Pten, or floxed Pten and floxed Trp53, at 25 weeks of age.

Patient-derived xenograft (PDX) model

Patient tumor samples to be used in PDX models were collected and processed by the University of Iowa College of Medicine Tissue Procurement Core under IRB# 200804792. Tissue collection and distribution was performed in accordance with the guidelines of the University of Iowa Institutional Review Board. Briefly, following collection tumor samples were placed in DMEM containing 5% FBS, 1X Pen/Strep, and 1% fungizone. For initiation of PDX tumors, patient tumor samples were processed by mincing until they passed through an 18 G needle easily. The cells were then suspended in a 1:1 mixture of DMEM (GIBCO) and Matrigel (Corning, 354230), and subcutaneously injected into 2 or 3 NOD.Cg-Prkdc^{scid} Il2^{rgtmWjl}/SzJ (NSG) (Jackson Laboratory) mice. For the propagation of samples, tumors were dissociated into single-cell suspensions and each mouse was injected subcutaneously with 1x10^6 cells. Single-cell suspensions were generated by placement of the tumor into a sterile Petri dish containing 10 mL collagenase IV solution (9 mL HBSS (Ca^{2+}- and Mg^{2+}-free), 1 mL collagenase IV (Worthington Biochemical Corp.), and 5 mM $CaCl_2$). The tumor samples were first minced and incubated for 1 hr at 37°C. Following this, samples were further digested in 10 mL 0.05% trypsin (at 37°C for 10 min), and passed through an 18 G needle 30 times, after which the suspension was filtered using a 70 μm cell strainer.

Tail-vein metastatic colonization model

GS689.Li cells expressing luciferase and eGFP were treated with blebbistatin (20μM, 3 hr) or DMSO. 1x10^6 cells of either treatment group were injected into the lateral tail-vein of 8-10 week-old male NOD-*Prkdc*^{em26Cd52}*Il2rg*^{em26Cd22}/NjuCrl (Charles River, 572) mice and tumor formation was monitored by bioluminescence imaging. Mice were considered to have metastatic lesions if the photons/second was above 10^7.

Tail-vein hemodynamic force model

Cells were labeled with 1 μM Cell-Tracker Green (Invitrogen; C7025) or Cell-Tracker Red (Invitrogen; C34552) and 2μg/mL Hoechst 33342 (Invitrogen; H1399) for 30 min prior to being mixed with 15-μm microspheres (Invitrogen; F8843) and suspended in PBS. A sample of the mixture was taken for the control to calculate the cell-to-microspheres ratio, after which 200 μL were injected into the tail vein of a 8-10 week-old male BALB/c mouse (Charles River). Mice were anesthetized with isoflurane immediately after injection and terminal cardiac blood collection was performed. Blood was placed in heparinized collection tubes (BD Microtainer, 365974) for further processing. The lungs were inflated by tracheal injection with a 1:1 mixture of OCT and PBS, mounted in OCT, and flash frozen. Lungs were then sectioned at 20-μm thickness and sampled at 200 μm intervals. Whole-lung sections were imaged. Cells were counted and the number of microspheres was calculated by image analysis as described below.

Orthotopic prostate xenograft model

5x10^4 GS689.Li cells (in 50μL) were orthotopically injected into the anterior prostate lobe of 8-13 week-old NSG mice using a 31G insulin syringe (BD, 328468). Injection was performed by locating and externalizing the anterior prostate and seminal vesicle through a midline incision. A successful injection was determined by localized fluid bleb in the prostate. After injection, the prostate and vesicle was placed back into the peritoneal cavity and midline incision closed. As described above, this cell line was derived from the PC-3 parent line by selection for cells that are highly metastatic *in vivo* (Drake et al., 2009). These cells were engineered to express luciferase and enhanced green fluorescent protein (EGFP), which allows for monitoring tumor burden and the detection of CTCs, respectively. Mice were randomized into two groups with similar tumor burden and injected intravenously with 50 μL of either 2.5 mg/kg (-)-blebbistatin or vehicle (15% DMSO, 85% PEG-400). Blood was collected 3 hr after injection by terminal cardiac puncture, and samples were analyzed by flow cytometry as described below.

METHOD DETAILS

Fluid shear stress assay

Cells were suspended in DMEM without FBS at a concentration of 5x10^{5}cells/mL and exposed to FSS at a flow rate of 250 μL/s in a 30 Ga ½'' needle using a 5-mL syringe and a PHD1000 syringe pump (703006). For cells expressing luciferase, viability was determined by bioluminescence imaging (Barnes et al., 2012). For cells that did not express luciferase, the CellTiter-Blue reagent (Promega) was used. In all cases, viability was determined by normalizing signal to the static control (pulse 0).

Chemical Reagents

Cells were treated with blebbistatin (20 μM, 3 hr) (Selleckchem, S7099), fasudil (5 μM, 24 hr) (Selleckchem, S1573), ML7 (20 μM, 1 hr) (Sigma, I2764), ionomycin (10 μM, 30 min) (Sigma, I9657), SMIFH2 (20 μM, 1 hr) (Sigma, 344092), CK-666 (50 μM, 1 hr) (Sigma,

182515), or staurosporine (4 μM, 4 hr) (Selleckchem, S1421) prior to exposure to fluid shear stress (FSS). For mouse studies, blebbistatin (-) (Selleckchem, S7099) was injected once intravenously, at a dose of 2.5 mg/kg.

Flow cytometry

Data were collected using a Becton Dickinson LSR II flow cytometer and analyzed using the FLOWJO platform (FLOWJO, LLC).

Evaluation of Membrane Repair

To detect damage to the plasma membrane, 1.75 μg/mL propidium iodide (PI) was added to a cell suspension before it was subjected to FSS. The size of plasma membrane disruptions was measured by adding 10 μM of 3, 10, 40, or 70 kDa FITC-dextran (LifeTechnologies; D1821, D3305, D1844, D1823) to the suspensions prior to FSS exposure. Samples were collected at "pulse 0" (static control), as well as immediately after pulses 1, 2, 5, and 10. They were washed with FACS buffer (1x PBS, 0.5% BSA, 0.1% NaN_3), centrifuged at 500 g for 3 min, then resuspended in the FACS buffer with 6 μg/mL Hoechst 33258 (Thermo Fisher; H3569) and either 2-μm YG microspheres (Polysciences; 17155-2) or 15-μm scarlet microspheres (Invitrogen; F8843). For calculating the percentage of cells in each fate, the ratio of intact cells to the counting beads was first calculated. For each pulse evaluated, the intact ratio was normalized to the static control sample (pulse 0). The normalized intact ratio was than multiplied by the percentage of cells for each fate ($PI^-Hoechst^-$, $PI^-Hoechst^+$, $PI^+Hoechst^+$, and $PI^+Hoechst^-$).

Staining for Annexin V

PC-3 cells were treated with DMSO or 4 μM staurosporine for 4 hr. Prior to FSS exposure (pulse 0), 500 μL samples were taken and assessed for Annexin V expression. The samples were washed with staining buffer (BioLegend, 420201), centrifuged at 500 g for 3 min, and resuspended in 100 μL of Annexin V Binding Buffer (BioLegend, 422201) with allophycocyanin (APC)-conjugated Annexin V (1:20; BioLegend, 640920) for 30 min. 400 μL of Annexin V binding buffer with Hoechst 33258 and 15-μm scarlet microspheres was added prior to analysis.

Staining for CD45

Non-tumor bearing male mice were treated with 2.5 mg/kg of either blebbistatin or vehicle. At 3 hr after treatment, blood was collected by terminal cardiac draw, and 500 μL of blood was mixed with 10 mL of red blood cell (RBC) lysis buffer (150mM NH_4Cl, 10mM $NaHCO_3$, 1.3 mM EDTA), centrifuged at 500 g for 3 min, and resuspended in FACS buffer. Samples were blocked in FACS for 30 min and incubated with anti-mouse CD45 (1:100, BioLegend 103110) for 1 hr. Samples were washed 3 times with FACS buffer and suspended to the volume initially collected, in FACS buffer containing a specific concentration 15-μm scarlet microspheres.

Analysis of circulating tumor cells (CTCs)

Blood samples collected for flow cytometry analysis were processed using RBC lysis buffer, centrifuged at 500 g for 3 min, then suspended to the volume initially collected, in FACS buffer containing either 2-μm YG microspheres (Polysciences; 17155-2) or a known concentration 15-μm scarlet microspheres. The initial concentration of the 2-μm YG microspheres was calculated using the known concentration of 15-μm scarlet microspheres. Hoechst 33258 was used to distinguish between live and dead circulating $EGFP^+$ tumor cells. The volume analyzed was determined by dividing the number of microspheres analyzed by their concentration (microspheres/mL) in the sample. The cell concentration (cells/mL) was calculated from the cell count and the volume analyzed. (Alexander et al., 2018)

Rho GTPase activity assay

For both the static and FSS-exposed samples, cells were released from the tissue-culture dish with 0.25% trypsin (GIBCO 25200-056), suspended in media containing FBS, centrifuged at 300 g for 5 min, resuspended in 5 mL of DMEM, and held in suspension for 30 min prior to exposure to two pulses of FSS at 250 μL/sec. Lysophosphatidic acid (LPA) positive controls were serum starved overnight in DMEM with 5 mg/mL bovine serum albumin (BSA), then treated with 5 μM LPA (Sigma, L7260) for 3 min prior to lysis. To detect GTP bound RhoA or RhoC, cells were lysed using Rho activity buffer (50mM Tris, 500mM NaCl, 50mM MgCl2, 1% Triton X-100, 0.1% SDS) and the volume was normalized such that 800-1000 μg of protein was used for each pulldown. To detect GTP bound RAC1, cells were lysed using RAC activity buffer (50mM Tris, 500mM NaCl, 50mM MgCl2, 1% Triton X-100) and 800-1000 μg of protein used for each pulldown. For each pulldown sample, 5% was saved for use as the input control and the rest was incubated with recombinant protein (Rho binding domain of Rhotekin for RhoA/C or of PAK1 for RAC1) (> 30 μg) for 45 min at 4°C. Samples were washed 3 times with 1 mL of RhoA activity buffer and centrifuged at 4°C and 500 g for 3 minutes.

Western blotting

Samples were loaded onto SDS-polyacrylamide gels (NuPage 4%–12% Bis-Tris Protein Gels, Novex) and transferred to PVDF membranes (Immobilon-FL), which were incubated in primary antibody (1:500 mouse anti-RhoA, ARH04, Cytoskeletal Inc.; 1:1000 mouse anti-β-tubulin, Developmental Studies Hybridoma Bank; 1:1000 mouse anti-Rac1 BD Bioscience; or 1:1000 rabbit anti-RhoC, D40E4, Cell Signaling) overnight. The blots were subsequently incubated with secondary antibody (1:10000 goat-anti-mouse; Rockland, 610-731-124; 1:10000 goat anti-mouse Jackson Labs, 715-036-151; or 1:20000 goat anti-rabbit LiCOR, 925-68071) and signal was assessed using either an Odyssey (LI-COR) or a ChemiDocX (BioRad) system.

Cortical F-actin measurement

To measure the density and organization of F-actin after FSS exposure, we exposed PC3 cells to 2 pulses of FSS. To identify dead and damaged cells, we added propidium iodide (1.75 μg/ml) to the cell suspension before FSS. Immediately following FSS, we fixed cells with 1% paraformaldehyde for 20 min. After washing with PBS, cells were stained with 1:500 phalloidin-AlexaFlour488 (ThermoFisher, A12379) and 1:500 DRAQ5 (ThermoFisher, 62251) in staining buffer (2% FBS in PBS, v/v) for 30 min. Cells were then washed with PBS and resuspended with 80 μL of staining buffer for imaging flow cytometry (ImageStream®X Mark II, EMD Millipore) at the UCLA Flow Cytometry Core Facility of Eli and Edythe Broad Center of Regenerative Medicine and Stem Cell Research. To quantify cortical F-actin levels, we used the ImageStream Data Analysis and Exploration Software (IDEAS) (Amnis Corporation). The cortical region was defined by subtracting the Erode mask (8 pixel) from the Dilate mask (1 pixel) of the brightfield channel.

Clonogenic Assay

GS689.Li cells were pretreated with either blebbistatin or DMSO for 3 hours at the indicated dose and then 300 (Figure S7D) or 1000 (Figure 5G) cells were seeded in 6-well dishes (ThermoScientific, 140675). Colonies were allowed to grow for 9-11 days before being fix with 70% EtOH and stained with Coomassie Blue R-250 (BioRad, 1610436). Colonies were counted with GelCount (Oxford Optronix).

Image analysis

Microscopy images were acquired using an Olympus BX61 or a Leica SP8 microscope. For imaging of the lung, a region of interest (ROI) encompassing the entire lung section was selected, and images were collected through 4 fluorescence channels and stitched together using microscope software (LAS X, Leica or cellSens, Olympus). Image analysis was performed using the FIJI software (Rueden et al., 2017). The threshold for the detection of fluorescent cells was set as signal > 4 standard deviations above the mean fluorescence intensity across the lung section. ROIs were selected using the analyze particle tool in FIJI. The presence of a nucleus in an area positive for cytoplasmic fluorescence was determined by measuring nuclear signal in the ROIs for the fluorescence channels corresponding to Cell-Tracker Red and Green; ROIs were considered to contain a nucleus only if the average signal was greater than the mean + 1 standard deviation of the fluorescent signal for the lung section in the nuclear (Hoescht 33342) channel. The percentage of intact cells lodged in the microvasculature was determined based on the ratio of cells to microspheres in the lungs at p2 versus p0 (pre-injection control sample).

Bioluminescence imaging

After orthotopic tumors were implanted, their growth was monitored to assess tumor burden by weekly bioluminescence imaging. Imaging entailed intraperitoneal injection of 150 mg/kg of D-luciferin (GoldBio, LUCK), followed 5 min later by the detection of bioluminescence using an AMI X imager (Spectral Instruments Imaging); exposure time was 5 minutes. The AMIView Imaging Software was used to select an ROI including the whole body for quantification of signal intensity.

Cell-free luciferase assay

Assay validation

To validate that cell-free luciferase measurements correlate with the destruction of cells due to FSS, we compared the calculated percentage of cells destroyed by exposure to FSS with the loss of viability as measured with bioluminescence signal (Figure S9). Specifically, luciferase expressing PC-3 cells were suspended in 90% DMEM and 10% ddH_2O and then subjected to FSS. To generate a standard curve, we lysed PC-3 cells at a concentration of $5x10^6$ cells/mL in 1% Tween-20 in ddH2O and subsequent dilution the lysate 1:10 with DMEM and measured the cell-free luciferase signal that correspond to 0, 25, 50, 75, and 100% of cells destroyed. We took 1 mL samples prior to and after 10 pulses of FSS exposure, centrifuged at 1,500 x g for 5 min, and the supernatants were transferred into new tubes. Subsequently, 100 μL aliquots were pipetted into wells of a 96-well black-bottom plate (Corning 3915) and 100 μL of assay buffer (200mM Tris-HCl pH = 7.8, 10mM MgCl2, 0.5mM CoA, and 0.3mM ATP, 0.3 mg/mL luciferin) was placed in each well to measure luciferase activity. The fractional cell viability as measured in luciferase assay of cells exposed to FSS was plotted against a standard curve of the cell-free luciferase signal generated from cell-lysate from a known quantity of cells.

Application of cell-free luciferase assay to mouse plasma

A standard curve was generated from data for $5x10^5$ cells lysed with 200 μL 1% Tween-20 in ddH2O. The standard curve was generated using samples in which lysates were titrated into 500 μL of freshly isolated mouse blood, corresponding to the destruction of $2.08x10^5$, $1.04 x10^5$, and $5.20 x10^4$ cells. Assuming that BALB/c mice have ~1.5 mL of blood (Vácha, 1975), these samples represent ~33% of the blood pool into which the cells were injected; this number was the basis of normalization of the luciferase signal obtained from the standard curve to the total blood pool. Both the blood for the standard curve and samples collected from mice injected with cells via the tail vein were centrifuged at 2,500 x g for 5 min. Subsequently, 100 μL of plasma was collected and combined with 100 μL of luciferase assay buffer (200mM Tris-HCl pH = 7.8, 10mM MgCl2, 0.5mM CoA, and 0.3mM ATP, 0.3 mg/mL luciferin) for measurement of the luciferase activity. Only blood collected from mice that had fully patent injections were used for analysis. The number of cells destroyed following tail-vein injection was assessed by simple linear analysis using the standard curve.

QUANTIFICATION AND STATISTICAL ANALYSIS

Data were analyzed using the statistical tests indicated in each figure legend; when appropriate, Bonferroni's correction for multiple comparisons was used. For each experimental group, the FSS assay was repeated at least 3 times over independent passages. For the F-actin data in Figure 3, the signal intensity was normalized to the median of the static control and presented as median with 95% CI error bars. The concentrations of CTCs and $CD45^+$ cells in Figure 6 are presented as medians and interquartile range, the flow analyses for undamaged and repaired in Figure S2 are presented as stacked bar charts of the component means, and all other data are presented as the mean with SEM indicated by error bars. Statistical significance was set at $p < 0.05$ and all statistical tests were two-sided.

DATA AND CODE AVAILABILITY

This study did not generate any datasets. Source data for figures will made available from the Lead Contact upon request.